BIOCHEMISTRY
including biophysical chemistry & molecular biology

Article

pubs.acs.org/biochemistry

Molecular Mechanism of Viral Resistance to a Potent Non-nucleoside Inhibitor Unveiled by Molecular Simulations

Shailendra Asthana,[†] Saumya Shukla,[‡] Paolo Ruggerone, and Attilio V. Vargiu*

Dipartimento di Fisica, Università degli Studi di Cagliari, Cittadella Universitaria, 09042 Monserrato, CA, Italy

Supporting Information

ABSTRACT: Recently, we reported on a potent benzimidazole derivative (227G) that inhibits the growth of the bovine viral diarrhea virus (BVDV) in cell-based and enzyme assays at nanomolar concentrations. The target of 227G is the viral RNA-dependent RNA polymerase (RdRp), and the I261M mutation located in motif I of the RdRp finger domain was found to induce drug resistance. Here we propose a molecular mechanism for the retained functionality of the enzyme in the presence of the inhibitor, on the basis of a thorough computational study of the apo and holo forms of the BVDV RdRp either in the wild type (wt) or in the form carrying the I261M mutation. Our study shows that although the mutation affects to some extent the structure of the apoenzyme, the functional dynamics of the protein appear to be largely maintained, which is consistent with the retained functionality of this natural mutant. Despite the binding site of 227G not collapsing or undergoing drastic structural changes upon introduction of the I261M substitution, these alterations reflect crucially on the binding mode of 227G, which is significantly different from that found in wt RdRp. In particular, while in the wt system the four loops lining the template entrance site embrace 227G and close the template passageway, in the I261M variant the template entrance is only marginally occluded, allowing in principle the translocation of the template to the interior of the enzyme. In addition, the mutated enzyme in the presence of 227G retains several characteristics of the wt apoprotein. Our work provides an original molecular picture of a resistance mechanism that is consistent with published experimental data.

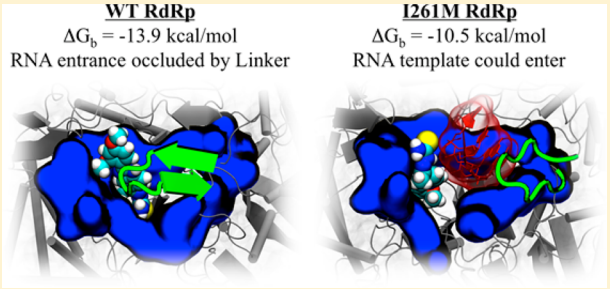

The bovine viral diarrhea virus (BVDV), which belongs to the *Pestivirus* genus of the Flaviviridae family, is the source of severe diseases in cattle and other ruminants,[1,2] having a huge impact on livestock worldwide.[3]

Although several vaccines against this pathogen are available,[4] they are most effective in preventing acute disease. Moreover, the heterogeneity of circulating BVDV strains hinders the prevention of fetal infections,[5] thus rendering the benefits of the vaccine unguaranteed with respect to fetal protection and prevention of fertility (these two factors have the greatest impact on economic losses caused by BVDV). In addition to vaccines, selective antiviral compounds have been developed; however, none showed high efficacy against this pathogen, and no drug has been marketed yet.[4] Thus, it is imperative to identify new lead compounds targeted at virus-specific steps of the replication cycle, to study their mode of action at the molecular level and, in parallel, to understand the mechanism exploited by resistant mutants to escape drug inhibition.

Recently, we reported on a 2-phenyl benzimidazole derivative [227G (Scheme 1)] that inhibits, in the low micromolar range, the multiplication of both BVDV and hepatitis C virus (HCV) in cell-based assays (EC_{50} values of 0.80 and 1.11 μM, respectively).[6,7] 227G has also been reported to inhibit, in enzyme assays, the recombinant RNA-dependent RNA polymerases (RdRps) of BVDV (IC_{50} = 0.002 μM) and HCV1b (IC_{50} = 0.4 μM).[7] To the best of our knowledge, the only other non-nucleoside inhibitor (NNI) described in the literature as being active against both BVDV and HCV is an imidazo-4,5-pyridine derivative,[8,9] although numerous other NNIs have been shown to inhibit BVDV by targeting its RdRp.[8−23] As with other NNIs, the 227G-resistant phenotype is characterized by the presence of a point mutation located in the finger domain (see Figure 1), namely I261M.[7] The occurrence of this mutation in the RdRp of resistant BVDV phenotypes had been already reported, coupled with either the N264D mutation [selected by 2-(4-acetylaminophenyl)-5,6-dichloro-1*H*-benzimidazole, compound 53][13] or the E291G mutation (selected by naphtyl azoenamine, compound 42).[19] However, the I261M mutation alone was reported for the first

Scheme 1. Chemical Structure of the Compound 2-{1-[2-(2,4-Dimethoxyphenyl)-1*H*-benzimidazol-5-yl]ethylidene}hydrazinecarbothioamide (227G)

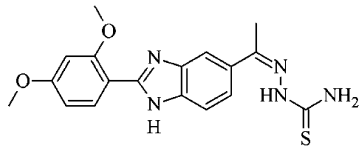

Received: April 24, 2014
Revised: September 15, 2014
Published: October 23, 2014

 © 2014 American Chemical Society dx.doi.org/10.1021/bi500490z | *Biochemistry* 2014, 53, 6941−6953

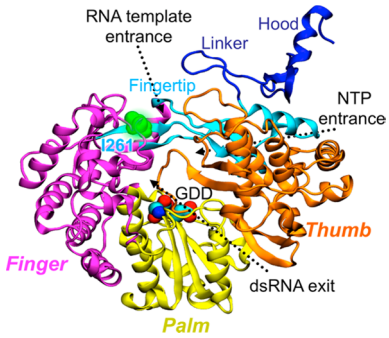

Figure 1. Structure of BVDV RdRp. The palm, thumb, and finger domains are shown as cartoons and colored dark yellow, orange, and purple, respectively, while the N-terminal and fingertip regions are colored blue and cyan, respectively. Residue I261 (on motif I of fingertip) is rendered as licorice and colored green, while the GDD catalytic triad is shown with van der Waals spheres colored according to atom type. The template and NTP entrances and the dsRNA exit sites are denoted by black dotted arrows.

time as an inducer of resistance to NNIs in ref 7. Residue I261 lies in the fingertip region [identified by residues R132−T162 and T259−I287 (see Figure 1)] of the finger domain, a key region for the polymerization reaction, as it contains motif I (A260−E265) and part of motif II (E281−Q308), both involved in binding of the incoming RNA template and NTPs.[16,24−26]

In ref 7, we discovered by computer simulations that 227G binds to the region lining the template entrance channel, where it stacks against motif I and is embraced by the four loops, L1 (P388−I398, finger domain), L2 (A221−N229, finger domain), L3 (A527−G537, thumb domain), and L4 or linker (L125−R132, N-terminal domain). Interestingly, I261 was found to have a key role in stabilizing the RdRp−227G complex.[7]

Here we address the molecular determinants of the I261M-induced resistance to 227G through an *in silico* comparison of the structural and dynamic behaviors of the apo and holo forms of the wild type (wt) and I261M variant of BVDV RdRps. We used a multidisciplinary computational approach that included flexible docking calculations, multicopy molecular dynamics (MD) simulations, calculation of 227G binding free energies, and estimation of the size and morphology of protein channels. Our data indicate that, although the I261M mutation induces appreciable structural changes into the apoenzyme, in particular in the putative region where 227G binds, these changes does not involve collapse or closure of the pocket. Furthermore, they are compatible with the retained activity of the apo mutant[7] and reflect crucially on the most stable binding poses of the inhibitor. Indeed, 227G binds to the surface of the template entrance channel of the 227G-resistant RdRp, where it sits within a subpocket different from (and adopting an orientation different from) that of its wt counterpart. Finally, the estimated affinity of 227G for the mutant RdRp, although lower than that calculated in the case of the wt RdRp−227G complex, is still within the submicromolar range. Therefore, the simple evaluation of the shift in affinity upon mutation could not provide sufficient information to determine the mechanism of resistance in this case. On the basis of the analysis of retained functional properties in the mutant RdRp, we depict a possible molecular mechanism of resistance that is in agreement with experimental data and compatible with a good affinity of the ligand for the enzyme. To the best of our knowledge, such a mechanism, in which a natural point mutation does not impair but only modifies to a minor (but crucial) extent the binding of a chemical, has never been proposed in the literature.

SYSTEMS AND METHODS

Systems. *Apoenzymes.* The X-ray crystal structure of BVDV RdRp (PDB entry 1S48, 3.0 Å resolution)[26] was used as a starting conformation for MD simulations of the apoenzymes (see Figure 1 for structural details of the protein). The wt apoenzyme will be termed APO hereafter. To model the mutant enzyme (hereafter APOm), the I261M substitution was manually inserted into the structure displaying the lowest root-mean-square deviation (RMSD) from the average extracted from the first 5 ns of MD simulation of APO, using VMD.[27]

The structure of 227G, not available from experiments, was taken from ref 7. Briefly, the molecule was first drawn with ACD Chem Sketch 11.0 (http://www.acdlabs.com). The resulting molecular structure was then optimized at the HF/6-31G(d) level up to a convergence in energy of 10^{-5} au using Gaussian03.[28]

Holoenzymes. Structures of the BVDV RdRps−227G complexes were generated through a robust docking protocol using AutoDock version 4.0.[29] More details about the docking protocol are reported below.

Methods. *MD Simulations.* All-atom MD simulations, in the presence of explicit water and counterions, were conducted with the NAMD package.[30] The AMBER99SBIldn, TIP3P, and AMBER-modified[31−33] force fields were used to model proteins, water, and ions, respectively. The GAFF force field[34] was used to describe the 227G structure, with charges calculated following the standard AMBER protocol: from the electrostatic potential map generated by the molecule (calculated with Gaussian03), RESP[35] charges were derived using the ANTECHAMBER module of AMBER. For all systems, the following procedure was used. First, geometry optimization was conducted with a two-step protocol: (i) 10000 cycles (2000 of steepest descent plus 8000 conjugate gradients) with harmonic restraint k = 10 kcal mol^{-1} Å^{-2} on each heavy atom of the solute and (ii) 10000 conjugate gradient cycles without restraints. Next, heating to 300 K was achieved by linearly increasing the temperature via constant-volume and -temperature MD for 100 ps, while imposing restraints of 1 kcal mol^{-1} Å^{-2} on the solute. Restraints were then released for 100 ps, and as a last step preceding the productive dynamics, constant-pressure and -temperature MD was conducted for 1 ns to relax the simulation box. Finally, 100 ns MD simulations were performed under the *NPT* ensemble. Overall, 10 such MD simulations, six of the apoenzymes and four of the complexes, plus two 5 ns MD simulations of the complexes were performed, for a total simulation time of ∼1 μs (*vide infra*). Because the dynamics of the wt and mutated apoproteins displayed significant differences at the putative binding region, which reflected on the most stable docking poses of 227G (see Results and Discussion), we decided to perform two additional simulations that were 1 μs in length, to ensure that the large-scale motions we have seen were truly representative of equilibrium dynamics. Pressure and temperature were regulated at 1 atm and 300 K using the isotropic Andersen−Parrinello−Rahman barostat[36,37] and the Nosé−Hoover thermostat,[38,39] respectively. Electrostatic interactions were evaluated using the soft particle mesh Ewald schemes[40] with a 1 Å grid spacing and a cutoff of 12 Å, the same used for Lennard-Jones interactions.

Chart 1. Computational Protocol Used in This Study (see Systems and Methods for a description)

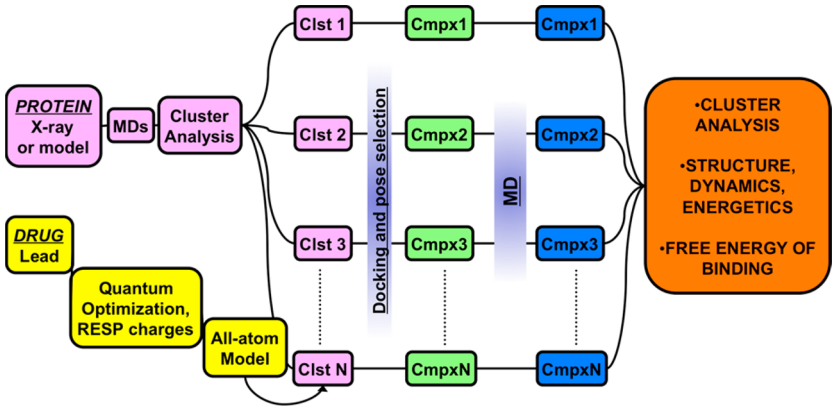

Docking. In ref 7, we obtained a concordance of results between guided and blind docking approaches in identifying the highest-affinity site of 227G on BVDV and HCV RdRps. In view of those results, we perform here docking calculations guided by previous experimental findings.[7,13,14,16,24,25,41] The side chains of key residues D126, R127, E128, A221, F224, I/M261, N264, S532, S533, and A392 were allowed to rotate during docking to account for the local flexibility of the protein. These residues include not only those in direct contact with 227G in the complex with wt BVDV RdRp[7] but also those that are lining the binding sites of other NNIs (namely, A221,[25,41] F224,[12,24,25,41] I261,[13,14,16,17] N264,[13,14,16] and A392[13,16,17,41]) and/or conferring resistance to compounds of this class or different classes upon substitution (F224,[24,25,41] I261,[13,14] N264,[13,16] and A392[13,16]).

Moreover, with respect to ref 7, we accounted to some extent for the global flexibility of the protein in docking calculations by selecting several relevant conformations of the apoenzymes from multicopy MDs. Our scheme (depicted in Chart 1) was inspired by the RCS protocol developed by McCammon and co-workers.[42] At first, we performed multicopy MD simulations of the two apoenzymes [APO and APOm (see the previous paragraph)]. Then we concatenated the parts of three trajectories produced for each protein in which the total rmsd displays a plateau [corresponding to the last 60 ns of each trajectory (see Figure S1 of the Supporting Information)], and we performed a cluster analysis to find the largest panel of different structures representing equilibrium conformations of the apoenzymes. Only the palm domain of the protein (Figure 1) was selected for structural alignment, to highlight the structural differences in the region where 227G is thought to bind. The clustering method developed by Daura et al.[43] and implemented in the *g_cluster* module of the GROMACS 4.0.7 package[44] was used, and the analysis was performed on the backbone atoms of the molecules using a cutoff of 2 Å for the rmsd. The representative structures of the top four clusters of APO and APOm (grouping more than 95% of the total conformations sampled along the trajectory) were selected for multiconformer molecular docking using the AutoDock 4.0 package.[29] Grid maps of 40, 40, and 40 points in the *x*, *y*, and *z* directions, respectively (0.375 Å from each other), were centered on residue 261 in both APO and APOm. The Lamarckian genetic algorithm was used to generate the poses. The global optimization started with a population of 150 randomly positioned individuals, a maximum of 2.5×10^7 energy evaluations, and a maximum of 2.7×10^7 generations. The mutation rate, crossover rate, and elitism parameters were set to 0.02, 0.80, and 1, respectively. For a local search, we applied pseudo-Solis and Wets algorithms with the default parameters. A total of 200 docking runs were performed, and a cluster analysis of the binding poses was conducted using an rmsd tolerance of 2 Å.

The best poses were selected on the basis of cluster population, energy score, and proximity to the mutation site.[7,14,16,24,25,41] The complexes fulfilling the criteria mentioned above were selected as starting structures for subsequent MD runs.

Postprocessing of MD Trajectories. Equilibrium trajectories collected from the production MD runs (180 and 120 ns for apo- and holoproteins, respectively) were used to assemble an inventory of the structural, dynamic, and energetic features of the systems.

Structure. The rmsd per residue was calculated to characterize the regions of maximal distortion among all systems and with respect to the X-ray structure of the protein. We tracked changes in the secondary structure along the MD using the polyview package[45] (Figure S2 of the Supporting Information). To give a description of the molecular mechanism of resistance, we followed our previous work[7] and estimated the area of the template entrance region along the equilibrium dynamics, by considering the triangle defined by Cα atoms of terminal residues R127, F224, and A392 of loops L4, L2, and L1 (Figure S3 of the Supporting Information), which are part of the template entrance region. In addition, we searched for channels connecting the template and NTP entrances of the BVDV RdRp, and the latter to the dsRNA exit, comparing their features on the X-ray structure reported in ref 26 to those in representative structures of each simulated system (namely, the structure with the lowest rmsd from the average and the top four representative cluster structures). For this purpose, CHUNNEL[46] was used with the following parameters: a grid size of 1 Å, a mesh technique for the generation of molecular surface, a probe radius of 1.4 Å, and a scaling factor of 0.9 to implicitly take into account protein flexibility.

The hydrogen bonds (HBs) between 227G and RdRps were counted using VMD imposing cutoffs of 3.2 Å for the donor−acceptor distance and 150° for the donor−hydrogen−acceptor angle.[47] Durable and transient HBs were defined as those with lifetimes above and below 20% of the MD simulation time, respectively.[47] During the dynamics, we observed the formation of alternate HBs between the 227G donors and acceptors and

dx.doi.org/10.1021/bi500490z | *Biochemistry* 2014, 53, 6941−6953

the surrounding key residues. Therefore, we calculated their average dynamic length (ADL).[48] Hydrophobic contacts (HpHs) were counted using a cutoff of 4 Å for nonpolar and charged atoms.

Dynamics. To characterize changes in protein flexibility, the root-mean-square fluctuations (rmsfs) were evaluated for each system. Moreover, to highlight possible resemblances and differences in the collective motions of the RdRp functional domains, we calculated the covariance matrices from the equilibrium trajectory and performed a principal component analysis (PCA).[49−51] In PCA, the covariance matrix is constructed, usually taking the three-dimensional positional fluctuations of Cα atoms from their ensemble average position (after least-squares fitting to remove rotational and translational motion). Diagonalization of the covariance matrix yields a set of eigenvectors and corresponding eigenvalues, which represent the direction and amplitude of the motion, respectively.[50] The eigenvectors are then ranked according to decreasing associated eigenvalues, such that the first eigenvector represents the largest contribution to the total fluctuation of the system. To visualize the motions represented by the eigenvectors, the structures from the trajectories can be projected onto each eigenvector of interest [principal component (PC)] and transformed back into Cartesian coordinates. The two extreme projections along each eigenvector can then be interpolated to create an animation or compared to understand which parts of the protein are moving according to that specific eigenvector and to what extent. Usually, (a combination of) the first few principal components are able to represent most of the collective motions (the "essential dynamics"[50]) occurring in an MD simulation among different domains of a protein. In this study, the PCs are compared in two ways. The directions of two eigenvectors generated from different ensembles (i.e., with and without an inhibitor) are qualitatively compared from visual observation of the corresponding motions (e.g., see Figure S4 of the Supporting Information). Quantitatively, eigenvector directions can be compared using the inner product of two vectors, with a value of 0 indicating orthogonal directions and a value of 1 indicating identical directions (e.g., see Figure S5 of the Supporting Information). A second approach is the quantification of similar essential dynamics by comparing the "amount of sampling" along common eigenvectors, namely by analyzing the range and distribution of ensemble projections along those eigenvectors (e.g., see Figure S6 of the Supporting Information).

Free Energy of Binding. To compare the binding free energies of 227G on the wt and mutant BVDV RdRps, MM-PBSA[52−54] calculations were performed using the so-called single-trajectory approach,[55] on 800 snapshots (one every 75 ps) taken from a single equilibrium trajectory of each complex. Compared to the (in principle more accurate) three-trajectory approach, in which separate MD simulations are performed for the complex, ligand, and receptor, this procedure reduces the impact of numerical errors associated with MD simulations on the evaluation of binding free energies and allows for a more direct evaluation of the standard deviations of the terms appearing in the quantity of interest.

The binding free energy (ΔG_{bind}) of each system was evaluated as follows:

$$\Delta G_{bind} = G_{com} - (G_{rec} + G_{lig}) \quad (1)$$

where G_{com}, G_{rec}, and G_{lig} are the absolute free energies of the complex (227G−RdRp), receptor, and ligand, respectively, averaged over the equilibrium trajectory. According to the MM-PBSA scheme, the free energy difference can be decomposed as $\Delta G = \Delta E_{MM} + \Delta G_{solv} - T\Delta S_{conf}$, where ΔE_{MM} is the difference in the molecular mechanics energy, ΔG_{solv} is the solvation free energy, and ΔS_{conf} is the conformational entropy. The first two terms were calculated with the following equations:

$$\Delta E_{MM} = \Delta E_{bond} + \Delta E_{angle} + \Delta E_{torsion} + \Delta E_{vdw} + \Delta E_{ele} \quad (2)$$

$$\Delta G_{solv} = \Delta G_{solv,PB} + \Delta G_{solv,SA} \quad (3)$$

E_{MM} includes the molecular mechanics energy contributed by the bonded (E_{bond}, E_{angle}, and $E_{torsion}$) and nonbonded (E_{vdw} and E_{ele}) terms of the force field. ΔG_{solv} is the solvation free energy, which has an electrostatic contribution ($\Delta G_{solv,PB}$, evaluated using the Poisson−Boltzmann equation) and a nonpolar one ($\Delta G_{solv,SA} = \gamma\Delta_{SA} + b$, proportional to the difference in solvent-exposed surface area, Δ_{SA}). The electrostatic solvation free energy was calculated using DELPHI,[56] with dielectric constants of 1 for the solute and 78.5 for the solvent. Atomic radii were taken from PARSE with an additional value of 1.90 Å for phosphorus, while partial charges were taken from the AMBER/GAFF force fields. The electrostatic potential was calculated on a cubic lattice with a length equal to 120% of the longest interatomic distance of the protein, using a grid spacing of 0.5 Å^{-1}. Ten thousand iteration steps were requested for the convergence of the energy (using the linear form of the PB equation). The surface area entering in the equation for $\Delta G_{solv,SA}$ was calculated using MOLSURF. In the evaluation of $\Delta G_{solv,SA}$, γ and b were assumed to be 0.00542 kcal mol^{-1} Å^{-2} and 0.92 kcal/mol, respectively, for use with PARSE atomic radii. The solvent probe radius was set to 1.4 Å.

The solute entropy contribution, ΔS_{conf}, is composed of a rototranslational term, calculated through classical statistical mechanics formulas, and a vibrational term, estimated by normal-mode analysis using the NMODE module of AMBER 9.0. To reduce the errors in the evaluation of the entropic term and to accelerate the calculation of the vibrational contribution to ΔS_{conf}, we followed a recently developed approach.[57] In the variant by Kongsted et al., normal-mode calculations are performed on a subset of atoms of the system (namely those of residues within 8 Å of the inhibitor), but in the presence of a buffer region containing protein residues between 8 and 12 Å from the inhibitor and water molecules within 12 Å of the ligand. This avoids large distortions of the structure with respect to the conformation extracted from the dynamics and avoids the use of a distance-dependent dielectric constant. The convergence cutoff on the force was set to 0.0001 kcal mol^{-1} Å^{-1}.

Per-residue contributions to the stabilization of the complexes were calculated by means of the MM-GBSA scheme.[53] The MM-GBSA approach furnishes an intrinsically easy way of decomposing the free energy of binding into contributions from single atoms and residues,[58,59] which is alternative to the "alanine scanning" approach implemented in the MM-PBSA scheme.

RESULTS AND DISCUSSION

To shed light on the mechanism of resistance to 227G caused by the I261M mutation in the BVDV RdRp, we used a multidisciplinary approach inspired by the RCS protocol developed by McCammon and co-workers.[42,60] Our scheme (Chart 1) combines docking calculations with multicopy MD

dx.doi.org/10.1021/bi500490z | Biochemistry 2014, 53, 6941−6953

simulations, free energy estimates, and identification of functional channels within the protein.

In the absence of experimental data for the structure of the RdRp−227G complexes, computational models require a thorough validation. In tune with this goal and knowing that docking algorithms are extremely sensitive to minor adjustments occurring within the binding site and that properly accounting for flexibility is crucial to obtaining reliable results,[42,60−65] we refined our strategy with respect to that used in ref 7. Here we accounted for backbone flexibility by using several configurations of the apoenzymes selected by a cluster analysis of the MD trajectories.

For the sake of clarity, we present the results according to the study sequence summarized in Chart 1. We start the section with a short overview of the main structural features of RdRp, followed by review and discussion of the results for the apoproteins. Then we describe the results of the docking procedure and the criteria chosen to identify starting structures for MD simulations of the holo complexes. Finally, a picture of how the mutation affects the binding and the activity of 227G is extracted from the whole corpus of computational data obtained in this work.

Structural Features of BVDV RdRp. The three-dimensional structures of RdRps from RNA viruses are significantly similar. They resemble a right hand[66,67] (Figure 1) in which three domains can be identified: finger, thumb, and palm. The BVDV RdRp is unique as it contains an additional structure, the fingertip, extending from the finger to the top of the thumb (linker + hood). The fingertip creates an "encircled active site" where important functions occur, such as RdRp dimerization and protein−protein interactions, allowing the assembly of an active replication complex, template and NTP binding, and template/product translocation.[66,67] Priming and elongation are conducted in the catalytic site present in the palm domain. The fingertip includes the terminal part of motif II (E281−Q308) and motif I (A260−E265), which contributes to the NTP binding site. The N-terminal domain follows, which includes the linker (L125−R132), responsible for recruiting other proteins during polymerization,[26,68−70] and the hood (V92−Q124), involved in dimerization.[26,68,70] The I261M mutation, object of our investigation, is located within motif I.

Apoproteins. *Structure.* A plateau in the total rmsd of the solute was reached within the first 40 ns of the MD trajectory for all the systems considered in this study (Figure S1A of the Supporting Information). The largest deviations with respect to the X-ray structure PDB entry 1S48 are localized in the N-terminal domain (residues V92−R132 in the structure with PDB entry 1S48[26]) and in the RNA−template binding region [loops L1−L4 and motif I (Figure S1C−E of the Supporting Information)], while the "scaffold" including the palm, thumb, and finger domains does not present relevant changes (Figure S1B of the Supporting Information).

Considering the whole protein, we found several structural clusters for both APO and APOm (Table 1). The top four clusters of each system were selected for further analysis as they cover more than 95% of the total sampled conformations (the top two clusters cover more than 85% of them). While in APO the backbone structures do not differ significantly among the clusters [all are relatively similar to the X-ray geometry, with values of the protein rmsd of <3 Å (Table S1 of the Supporting Information)], in APOm they feature two main conformational subgroups. These subgroups differ particularly in the position of the linker and the L2 loop (Figure 2) and exhibit relevant

Table 1. Clustering of Protein Trajectories[a]

	APO	APOm	COM	COMm
cluster 1	71.9	67.4	52.8	48.4
cluster 2	16.6	23.7	21.2	41.1
cluster 3	10.7	5.6	17.5	7.7
cluster 4	0.4	2.6	16.0	1.5
cluster 5	0.2	0.7	3.8	0.6
cluster 6	0.1	–	0.5	0.5
cluster 7	–	–	0.1	0.1

[a]Clustering of protein structures performed for each system over the equilibrated trajectories [180 (3 × 60) ns and 120 (2 × 60) ns for apo- and holoproteins, respectively]. In each system, two main clusters were found grouping together more than 70% of all conformations, while 95% of conformations are contained in the first four clusters. The corresponding representative structures of clusters 1−4 for each system are shown in Figure 4 and Figure S12 of the Supporting Information.

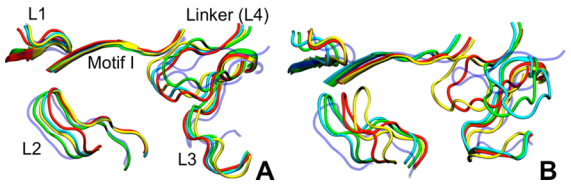

Figure 2. Conformation of the four loops (L1−L4) and motif I, lining the binding site of 227G, in the top four cluster representatives extracted from MD trajectories of (A) APO and (B) APOm. The first, second, third, and fourth most populated clusters are colored red, green, yellow, and cyan, respectively, while the X-ray structure is shown in transparent blue.

distortion from the X-ray structure of the wt protein (up to ∼2 Å larger than APO for the entire protein). Consistently, the rmsd difference between the average structures of APO and APOm is 3.9 Å, and even larger values are found for the hood and the linker (Table S2 and Figure S7 of the Supporting Information). Furthermore, these findings, as well as those described in the next paragraphs on apoproteins, were confirmed in two additional MD simulations, one of APO and one of APOm, each being 1 μs in length (see Figure S8 of the Supporting Information). Finally, these structural differences arise with no major changes in the secondary structure of APO or APOm (Figure S2 of the Supporting Information).

Dynamics. To highlight the regions featuring the largest changes in flexibility, we calculated the rmsf values of the Cα atoms for each residue and compared them to the calculated *B* factors taken from the X-ray structure (Figure S9 of the Supporting Information). The fluctuations calculated from MD simulations of APO compare quite well with those extracted from the X-ray structure. In particular, the peaks found in correspondence of the L3 and linker loops are conserved, while the hood features much higher flexibility along the MD trajectory than in the crystallographic structure. The latter finding, however, does not contrast with experimental results: indeed, Choi et al.[26] reported that this domain adapts its structure to different crystal forms, which reflects its high degree of conformational freedom. It is worth noting that this high mobility of the hood is retained upon mutation. Moreover, APOm fully conserves the rmsf peaks at L3 and at the linker loops as well as the intrinsic flexibilities of motifs I and II (Figure S9 of the Supporting Information). Additionally, the collective motions of the protein are also fairly conserved upon

dx.doi.org/10.1021/bi500490z | *Biochemistry* 2014, 53, 6941−6953

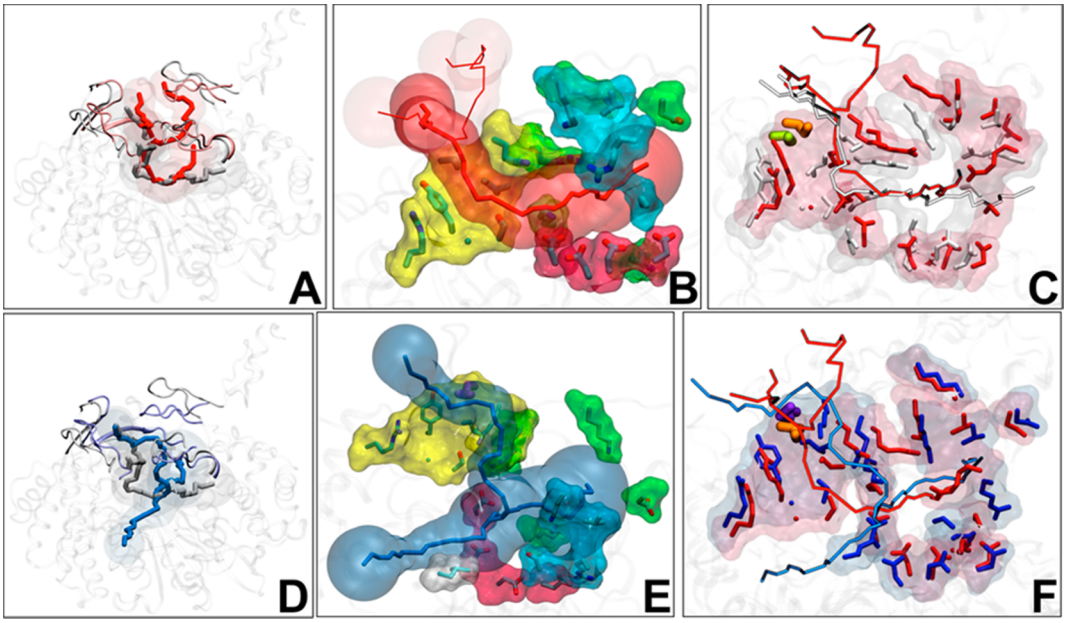

Figure 3. Channels found in APO (top panel, red sticks) and APOm (bottom panel, blue sticks) and in the X-ray structure (both panels, gray sticks). The structures featuring the lowest rmsd from the average were used for the calculation. Views are different for each picture to clearly highlight main findings. (A) The water paths connecting the template and NTP entrance sites are present in both APO and X-ray structures. The loops lining the template entrance are depicted as cartoons in solid colors, while the rest of the protein is transparent. (B) Close-up of the paths in APO. The path closest to that found in the X-ray structure is shown with thicker sticks. A transparent surface (darker for the path identified by thicker sticks) built with the radii of the channel (see Figure S10 of the Supporting Information) is also present. Key residues involved in the polymerase activity are drawn as sticks colored according to atom type and surrounded by molecular surfaces colored according to the region they line: the catalytic site (red), the priming site (cyan), the template entrance (yellow), and the NTP entrance (green). (C) Superimposition of APO (red) and X-ray (gray) structures showing the key residues (lining the main channel path). Residue I261 is shown as thicker sticks (orange for APO and yellow for X-ray). (D) Comparison of paths between the APOm (blue sticks) and X-ray structure. An additional path leading to the dsRNA exit is also present in APOm. (E) Close-up of the paths found in APOm. In addition to the key regions defined in panel B, there is an additional residue (L677, white transparent surface) lining the C-terminus. (F) Superimposition of APO (red) and APOm (blue) channels.

mutation (Figures S4 and S5 of the Supporting Information). Via comparison of APO and APOm, the first three PCs, which represent ∼80% of protein's "essential dynamics",[50] display an overlap between 0.4 and 0.6 (Figure S5A of the Supporting Information). The corresponding collective motions involve mainly the hood region, the thumb domain (relative to the palm and finger domains), and loops L3 and L4 (linker) (Figure S4A−C of the Supporting Information).

Functional Channels within RdRp. An active state of the RdRp requires the presence of the RNA template and NTP channels, both leading to the catalytic site, as well as of the channel allowing the exit of the dsRNA product[66,68,71,72] (the three entrance−exit sites are indicated in Figure 1). These paths are lined by key residues involved in the process of polymerization, which lie at different functional sites of the protein: the catalytic site (residues D345, D350, D448, and D449), the priming site (S498, R517, V521, and K525), the template entrance (I261, K263, R285, I287, Y289, R295, and G406), the NTP entrance (K172, D271, S282, R285, and K347), and the dsRNA exit at the C-terminus (L677).[26,66,68,71,72] We traced the channels present in representative average structures of APO and APOm and, for comparison, in the RdRp X-ray structure (Figure 3). In the X-ray structure, we identified the two entrance channels (template and NTPs) as being open, while the dsRNA exit channel is closed (Figure 3). This is consistent with literature data,[73] which suggest that the exit channel opens during the transition from the first and dinucleotide primer state to processive RNA synthesis along the replication process. In APO, the channel connecting the template and NTP entrance sites is very similar to that found in the X-ray structure (Figure 3A−C; see also Figure S10 of the Supporting Information) and, like the latter, is surrounded by the key residues of the catalytic, priming, template entrance, NTP entrance, and dsRNA exit functional RdRp regions.[26,66,68,71,72] Moreover, as in the X-ray structure, no channel was found going through the dsRNA exit site, which also remains closed in our simulations of the wt apoprotein.

Unlike APO and the X-ray structure, APOm features, in addition to the channel connecting the template and NTP entrance sites, another channel branching off from the former and leading to the dsRNA exit site (Figure 3D−F). Despite the path not being exactly superimposable with those of APO or the X-ray structure, it still goes through key residues of the RdRp functional regions involved in polymerization (Figure 3D).

To implicitly take into account the dynamic nature of RdRp at work, the same calculations were performed on representative structures of the four top clusters listed in Table 1 (Figure S11 of the Supporting Information). These data confirm the results found on representative average conformations and are in accordance with the retained functionality of the mutated enzyme, as suggested by the capability of the 227G-resistant mutants to replicate at high titers in MDBK cells.[7]

Docking of 227G on APO and APOm. The effect of the I261M mutation on the apoenzyme is most evident in the interaction of the protein with 227G. Figure 4 shows the conformations of the best poses (see also Table S3 of the Supporting Information) found by docking 227G on the

dx.doi.org/10.1021/bi500490z | *Biochemistry* 2014, 53, 6941−6953

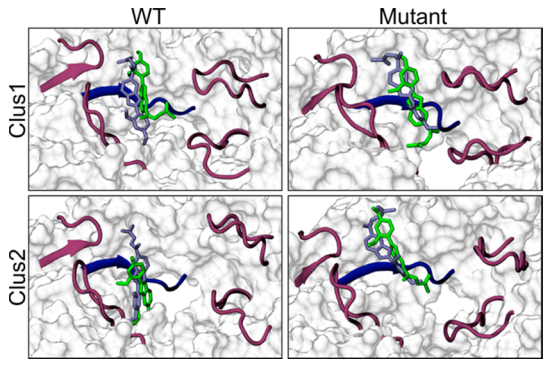

Figure 4. Highest-score docked poses of 227G in the binding pocket of BVDV RdRp. Structures of the wt and mutant proteins are representatives of clusters 1 and 2 extracted from MD trajectories of APO and APOm, respectively. The protein is rendered as a white molecular surface, with four loops and motif I highlighted as a cartoon (magenta and blue, respectively). The inhibitor is shown as sticks, and orientations 1 (with the phenyl group pointing upward) and orientation 2 (opposite of orientation 1) are colored green and ice blue, respectively.

representatives of the top two clusters extracted from APO and APOm dynamics (Figure 2; see Figure S12 of the Supporting Information for the poses of 227G on the third and fourth clusters of APO and APOm). Within the binding pocket, we identified two different orientations of the ligand (named Ori1 and Ori2) for each cluster representative structure (see Systems and Methods for selection criteria); the sole exception was cluster 3 in APO, where only one orientation was found. For subsequent MD simulations, we selected two representative structures for each protein and for each orientation of the ligand, out of the initial 15 structures [eight complexes in total (see Figure 4 and Figure S12 of the Supporting Information)]. We chose clusters 1 and 2, which group almost 90% of the conformations assumed by the apoenzymes during our MD simulations (Table 1). The following additional reasons led to this choice. (a) The conformation of the binding region differs significantly between the first two clusters (Figure 2; see also Table S4 of the Supporting Information). (b) In APOm, the first two clusters represent two conformational subgroups of the linker and loop L2, with clusters 3 and 4 being closer to clusters 1 and 2, respectively (Figure 2; see also Table S4 of the Supporting Information). Thus, our choice allowed us to investigate, with a reasonable computational effort, the effect of different starting orientations of 227G and different conformations of the loops on the conformation and dynamics of the complexes. Note that, although the possibility that a third different starting conformation could lead to different dynamics on the explored time scales cannot be excluded *a priori*, the results presented here furnish a molecular explanation of resistance, which yields a plausible rationale for the enzyme assay data.[7]

Interestingly, the ligand is unable to form a stable complex in clusters 1 and 2 of APO or in cluster 1 of APOm upon assuming orientation Ori2; in fact, 227G detaches from the binding site after a few nanoseconds (data not shown). As far as APO is concerned, the result is in agreement with previous work in which a single conformation of the protein was used for blind and focused docking calculations.[7] On the other hand, in the case of APOm, 227G was not stable in cluster 2 upon assuming orientation Ori1. Indeed, 227G flipped by ∼180° after ∼3 ns, assuming orientation Ori2 (data not shown). Summarizing, four adducts were stable along the 100 ns all-atom MD simulations (see Figure S13 of the Supporting Information): $APO_{clus1}{\cdot}227G_{ori1}$ (hereafter COM), $APO_{clus2}{\cdot}227G_{ori1}$ (hereafter COM′), $APOm_{clus2}{\cdot}227G_{ori2}$ (hereafter COMm), and $APOm_{clus1}{\cdot}227G_{ori1}$ (hereafter COM′m). Note that only in the case of the mutant are two possible orientations of 227G stable (Ori2 in COMm and Ori1 in COM'm), while in the wt RdRp, 227G assumes only orientation Ori1 in both COM and COM′. This is the first indication that the mutation strongly affects ligand−protein interactions.

Wild-Type versus Mutant RdRp−227G Complexes. The interaction of 227G with wt and mutant RdRps and the influence of the inhibitor on structural and dynamic properties of the binding site were clarified by analyzing MD trajectories. In the following, we focus on the comparison between COM and COMm. Very similar results were found for COM′ and COM′m, as outlined at the end of the section.

We first analyzed the rmsd profiles along the trajectories (Figure S1 of the Supporting Information) to assess the overall

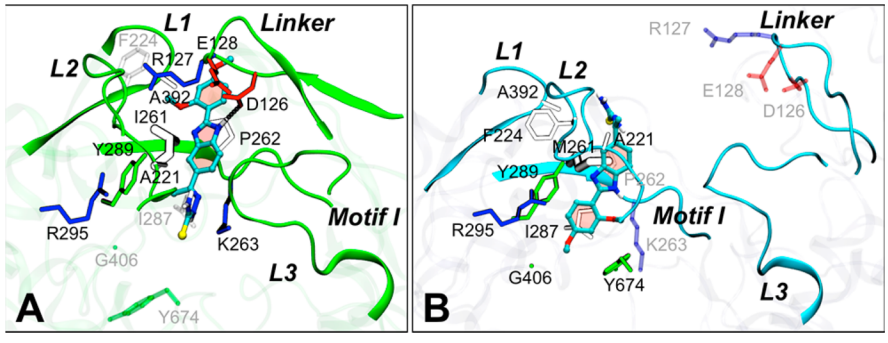

Figure 5. Pattern of interaction between 227G and RdRp as found in (A) COM and (B) COMm. Loops L1−L4 and motif I are highlighted with solid colors, and the rest of the protein is rendered as transparent. In both panels, only the residues (side chain nonhydrogenous atoms) within 5 Å of 227G are shown as sticks. Residues making favorable interactions are represented as solid sticks with black labels, while the other residues are shown as transparent sticks with gray labels. The residue coloring code is according to type: acidic, basic, polar, and hydrophobic amino acids colored red, blue, green, and white, respectively. HBs are shown with black spirals. In panel A, the favorable interactions with 227G are made by residues from all four loops and motif I. Four of them (A221, I261, P261, and A392) form hydrophobic interactions. Three (R127, R295, and K263) are positively charged. Two (D126 and E128) are negatively charged. One (Y289) is polar. A stable HB is formed between 227G and D126. In panel B, the orientation of 227G is the opposite of that in COM. In total, nine residues make favorable interactions with 227G: five hydrophobic (A221, F224, M261, I287, and A392), three polar (Y289, G406, and Y674), and one basic (R295).

dx.doi.org/10.1021/bi500490z | *Biochemistry* 2014, 53, 6941−6953

structural stability of the systems. As expected, the most stable profiles are those of COM. This is particularly true for the linker, which displays an almost flat profile after a first displacement of ∼6 Å. In contrast, rmsds of the N-terminal domain and linker in COMm display oscillations similar to those found in APOm. This different mobility of the linker is consistent with a very different interaction pattern established by 227G with the protein in COM and COMm, which can be seen from Figure 5. Thus, the aforementioned initial increase in the rmsd of this loop in COM corresponds to its displacement toward 227G, with which strong and durable contacts are formed. Consistent with previous findings,[7] in COM the inhibitor binds within a cavity encircled by loops L1−L4, and its benzimidazole moiety stacks against motif I. Despite slight differences with respect to our previous work (somewhat expected because of the different docking protocol and MD simulation times), the essential features of the RdRp−227G interaction, involving in particular residues of linker and motif I, are retained (Figure 5). Vice versa, in COMm the charged residues on linker and L3 loops are unable to form stable contacts with 227G, which is packed on one side of the template entrance between loops L1 and L2 and motif I only and is more exposed to the solvent (Figure 5B and Figure S14 of the Supporting Information). The different conformational changes induced in the binding region by 227G are better appreciated in Figure 6A−C, where representative conformations of the systems in pairs are compared. While in APO and COM both the linker and L3 loops undergo a significant movement toward 227G [>10 Å for the linker (Figure 6A)], in COMm the linker does not come in contact with the inhibitor (Figure 6B). The result is a drastic difference in the structures assumed by the binding regions of COM and COMm (Figure 6C), which is particularly noticeable in the area around the entrance of the RNA template channel [Figure 6D (see the next section)]. Furthermore, as will be shown at the end of this section, the findings described above are independent of the initial conformations of the RdRp−227G complexes.

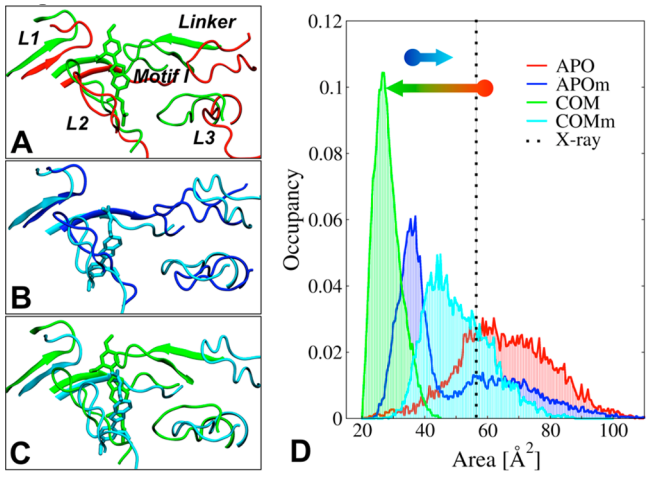

Figure 6. Comparison among the structures of the 227G binding region in APO, APOm, COM, and COMm (red, blue, green, and cyan, respectively). In all three pairs [(A) APO vs COM, (B) APOm vs COMm, and (C) COM vs COMm], the major differences are spotted in loop L4 and in the orientation of 227G. (D) Normalized distribution of the area enclosed by loops L1, L2, and L4 lining the template entrance site, evaluated over equilibrium trajectories. The dashed vertical line indicates a value of 56.4 Å calculated for the X-ray structure (black). The distribution of the area is unimodal in APO (red), with most likely values slightly below that found in the X-ray structure. In COM (green), the distribution becomes much narrower and is centered at ∼21 Å. The situation is opposite in APOm (blue), where a bimodal distribution with most likely values at around 40 Å (but a significant population at the same values as in APO) is found, while in COMm (cyan), the distribution is shifted toward a larger value with a peak at ∼50 Å.

To quantify the effect of the I261M mutation on the affinity of 227G for the RdRp, we evaluated the binding free energies of the ligand in COM and COMm and dissected ΔG_B into contributions from hydrophobic and polar terms, entropy (Table 2), and key residues of the binding region (Table S5 of the Supporting Information). Table 2 offers a useful comparison of the driving binding forces of 227G with wt and mutant RdRps. First, in both the cases, 227G binding is mainly driven by hydrophobic interactions. The less favorable $\Delta G_{solv,PB}$ term in COM, compatible with a higher degree of burying of the ligand, is more than compensated by the larger enthalpic terms ΔE_{ele} and ΔE_{vdw}. The conformational entropy cost is larger in COM, as expected from the better packing of the inhibitor in the wt enzyme. Summarizing all components, we find the binding free energy of COM is −13.9 ± 3.1 kcal/mol, in good agreement with previous findings[7] and with the value of −12.0 kcal/mol calculated from the experimental IC_{50} value (0.002 μM). The binding free energy of 227G in COMm is −10.5 ± 2.1 kcal/mol. A source of destabilization in COMm is the loss of interactions of the ligand with the linker and L3 loops, while motif II residues contribute more than in COM to form a stable adduct (Table S5 of the Supporting Information). Interestingly, in COMm the only residue of motif I that makes favorable interactions with 227G is M261, i.e., the mutated residue, and its effect is comparable to the contribution of I261 in COM. Therefore, although the ΔG_B value in COMm is lower than that found in COM, the affinity of 227G for the mutant is still in the submicromolar range. On the basis of these results, and apart from intrinsic limitations of the MM-P(G)BSA approach in evaluating absolute free energies of

Table 2. Experimental and Calculated Binding Free Energies for Binding of 227G to COM and COMm RdRps[a]

	COM	COMm
ΔE_{ele}	−25.2 (1.5)	−19.3 (2.3)
ΔE_{vdw}	−47.2 (3.9)	−39.9 (2.8)
$\Delta G_{solv,PB}$	44.1 (2.2)	36.7 (3.7)
$\Delta G_{solv,SA}$	−5.8 (1.7)	−5.6 (1.9)
PB_{tot}	−34.1 (3.8)	−28.1 (4.3)
$\Delta G_{ele+solv,PB}$	18.9 (3.9)	17.4 (3.2)
$\Delta G_{vdw+solv,SA}$	−53.0 (5.1)	−45.5 (4.3)
$-T\Delta S_{solute}$	20.2 (3.4)	17.6 (2.8)
ΔG^b	−13.9 (3.1)	−10.5 (2.1)
ΔG^c	−12.0	NA[e]
$IC_{50}{}^b$	7×10^{-5} [$(3 \times 10^{-7})/10^{-2}$]	2×10^{-2} [$(7 \times 10^{-4})/0.83$]
$IC_{50}{}^d$	2×10^{-3} (4×10^{-5})	NA[e]

[a]Energies are in kilocalories per mole, and all IC_{50} values are in micromolar. The experimental values of ΔG_{bind} are estimated from IC_{50} data with the equation $\Delta G_{bind} = RT \ln(IC_{50})$ (R is the universal gas constant, and T = 298.5K), while the calculated values are given by the formula $\Delta G_{bind} = \Delta E_{ele} + \Delta E_{vdw} + \Delta G_{solv,PB} + \Delta G_{solv,NP} - T\Delta S_{conf}$. PB_{tot} corresponds to the enthalpic term, which is equivalent to $\Delta E_{ele} + \Delta G_{solv,PB}$ and $\Delta E_{vdw} + \Delta G_{solv,SA}$ (see Systems and Methods for more details). [b]Calculated value. [c]Extracted from IC_{50}. [d]Experimental value. [e]Not available.

dx.doi.org/10.1021/bi500490z | Biochemistry 2014, 53, 6941−6953

binding,[52,53,58] we hypothesize a molecular mechanism of resistance compatible with the high affinity of 227G for the mutant RdRp. Insights into this topic came from a thorough analysis of trajectories, in terms of changes in secondary structure, local and global flexibilities, and properties of the RNA template and NTP entrance areas and of the dsRNA exit area.

First, the comparative analysis of secondary structures reveals notable differences only between the X-ray structure and COM (Figure S2 of the Supporting Information). Namely, a loss of α-helix and β-sheet charactes is observed in the hood and fingertip of COM, while the linker exhibits major distortions caused by newly formed β-sheet. This is consistent with the heavy structural and dynamical perturbation induced by 227G in the wt enzyme.

Second, the mobility of the binding region in the complexes, evaluated through the rmsf of the protein's Cα atoms and compared to experimental *B* factors, is strongly affected by the mutation (Figure S9 of the Supporting Information). In particular, two peaks corresponding to the positions of the linker and L3 loops are clearly seen in the rmsf profiles of all systems except COM. Also, the flexibility of motifs I and II is significantly lower in COM than in other systems. On the other hand, the rmsf profile of COMm is very similar to that of APO, particularly in the aforementioned key regions. Thus, the linker fluctuates in the X-ray structure and in all simulations except COM, where its flexibility is limited by the tight binding to 227G, and the mutation partially restores the natural behavior of this loop (see APOm vs COMm in Figure 6B). The flexibility of the linker is thought to be important for polymerization activity,[26,68−70] because this loop is supposed to escort the template into the catalytic site and to be involved in the recruitment of other proteins during polymerization.[68,69] Thus, the recovery of flexibility of this part of the protein upon mutation is consistent with the maintained functionality of the protein.

Third, the different impact of 227G on the dynamics of the wt and mutant RdRps is evident via a comparison of the amount of conformational overlap between the apo- and holoenzymes (Figure S4 of the Supporting Information) and the inner products between the eigenvectors of covariance matrices (Figure S5 of the Supporting Information). For instance, only four inner products larger than 0.5 are found between APO and COM (Figure S5B of the Supporting Information); moreover, the corresponding movements are localized in the hood, as this is the sole region involved in collective motions along the principal components of COM (Figure S4D−F of the Supporting Information). None of the aforementioned inner products correspond to overlapping movements in the binding region, which are frozen in COM. In contrast, the mutant RdRp retains a significant part of the functional collective movements upon binding of 227G (Figure S5C of the Supporting Information) and features the maximal overlap between the essential dynamic spaces (Figure S6 of the Supporting Information). Six inner products among the top four eigenvectors are larger than 0.5, and three diagonal inner products are larger than 0.5. Furthermore, in addition to the hood, the linker and L3 loops maintain collective and extended motions in COMm, which are similar to those found in APOm, and in some cases, the overlap extends to all four loops and to motif II (Figure S4G−L of the Supporting Information). Again, this supports retained conformational dynamics upon binding of 227G in the mutant. In view of these results, it is not surprising that only the second eigenvectors of COM and COMm (Figure S5D of the Supporting Information) show a consistent overlap, which is restricted to movements in the hood. Two inversions are seen between eigenvectors 1 and 3, the latter involving significant movement of only the thumb domain in COM (Figure S4M−O of the Supporting Information).

Comparison of RNA Template Entrances and RdRp Channels. The fourth and probably more interesting point concerns the comparison of the morphology of the functional protein's channels in wt and mutant RdRps. We first analyzed the distributions of the area enclosed by loops L1, L2, and L4 in COM and COMm (Figure 6D and Figure S3 of the Supporting Information). Despite our estimate being a rough approximation of the real value (see System and Methods), it gives a valuable indication of the different impact of the 227G binding on the structure and dynamics of the two proteins. The unimodal distribution in APO, with values slightly above that found in the X-ray structure (56.4 Å), indicates that there would be enough space for the template RNA to fit within the entrance loops. Upon binding of 227G (COM), the distribution becomes much narrower and centered at ∼28 Å, which is consistent with the hypothesized occlusion of the template entrance site.[7] A similar mechanism has been proposed for the inhibition of the Dengue RdRp by the NNI NITD-29,[74] although no structural insights were given thereon. Thus, we compared the apo and holo RdRps of Dengue and BVDV. The average backbone rmsd between the X-ray apo structures (PDB entries 2J7U[75] and 1S48[26] for Dengue and BVDV, respectively) is 1.31 Å. If we consider their complexes with the respective inhibitors (NS5-NITD29 cocrystal structure in ref 74 and the structure with the lowest rmsd from the average for COM), the rmsd is 1.46 Å, indicating that the structural similarity of the two proteins is retained upon binding of the inhibitors. In addition, in both cases the key residues for the RdRp−ligand interactions are those of the areas of the template entrance channel (Figure S15 of the Supporting Information), suggesting a similar mechanism of Dengue and BVDV RdRps inhibition.

The situation in the mutated protein is completely different. First, a bimodal distribution is found in APOm, with the most likely value at ∼35 Å but a significant population at values overlapping with those observed in APO (the two peaks correspond to the two main conformational subgroups clearly visible in Figure 2B). Second, the binding of the inhibitor to APOm causes a shift in the distribution toward larger values of the area: COMm features a peak at ∼47 Å (closer than APOm to APO) and a population of values more significant than that of APOm in the range of 50−70 Å (Figure 6D). These findings are consistent with the retained activity of the I261M variant of BVDV RdRp and with the ability of this virus to grow in the presence of 227G.

Despite the consistency between the analysis of entrance areas and the experimental evidence, it is important to remark that the agreement could be restricted to the area defined above, and a bottleneck for the RNA template could be induced by the mutation deeper inside the entrance channel, as well as in the NTP entrance and dsRNA exit channels. For this reason, we also performed an analysis of the (occurrence and size of) channels connecting the NTP and template entrances, and the latter to the dsRNA exit. Indeed, the active state of the polymerase requires the presence of the template and NTP channels,[66,68,71,72] both leading to the catalytic site (Figure 1).

dx.doi.org/10.1021/bi500490z | *Biochemistry* 2014, 53, 6941−6953

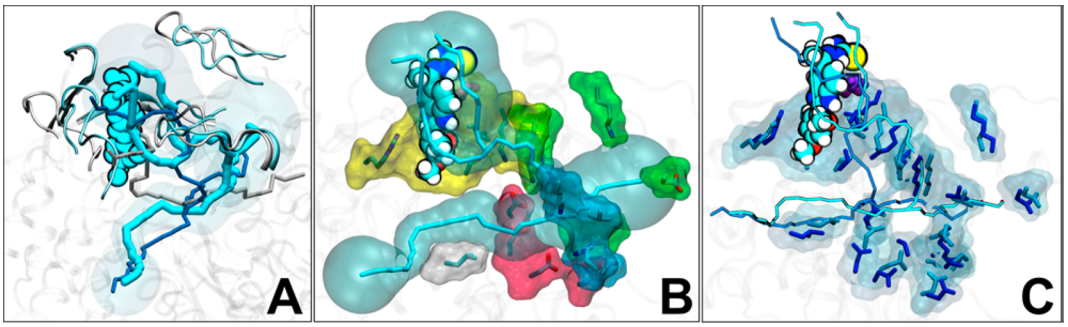

Figure 7. (A) Water channels found in representative average structures of COMm (cyan sticks), compared to those found in the X-ray (gray sticks) and APOm (blue) structures. For further details, see the legend of Figure 3. (B) Close-up of the paths found in COMm. (C) Superimposition of COMm (cyan) and APOm (blues) structures and channels, showing the relative conformation of key residues (lining the main channel path).

To take implicitly into account the dynamics of the protein, we calculated the morphology of the aforementioned channels in both the structures with the lowest rmsd from the average (Figure 7) and in the representatives of the top four clusters of each system (Figure S11 of the Supporting Information). In COM, no channel was found in any of the structures, while in COMm, the situation was found again to be totally different. In Figure 7A, it can be seen that, despite some differences with respect to X-ray and APOm, both the template and NTP entrances are interconnected between them and to the dsRNA exit, which is also open. In fact, two channels were found starting at the template entrance (merging into a single one within the protein) with radii of 4−6 Å (Figure S10 of the Supporting Information), in qualitative agreement with the estimate of the area reported above (Figure 6D). Also, at the NTP entrance site, the radius of the channel is similar to that found in the apoenzymes (Figure S10 of the Supporting Information). Finally, despite the size of the channel in the center being slightly smaller in COMm (and APOm) than in APO, the path is lined by all the key residues involved in polymerization,[26,66,68,71,72] which belong to the catalytic site, the priming site, the template and NTP entrances, and the dsRNA exit (Figure 7B). Upon interaction with the RNA template and/or NTP, large conformational changes are likely to occur in the protein, which should further open the channels. As shown in Figure 7C, good overlap between APOm and COMm is also found for the conformations of the aforementioned, functionally relevant residues lining the channels, which again is consistent with the retained polymerase activity of the mutant RdRp. The results outlined above are confirmed by the analysis of the structures of the top four clusters extracted from the dynamics of COMm (Figure S11C of the Supporting Information).

COM′ versus COM′m. As mentioned at the beginning of this section, two additional simulations were performed in this work for COM′ (APO_{clus2}·$227G_{ori1}$) and COM′m ($APOm_{clus1}$·$227G_{ori1}$). They show that the results presented so far are, in their essence, retained upon changes in the initial mode of binding of the ligand and pinpoint a striking difference in the interaction between 227G and the mutant enzyme with respect to the wt complex, which is crucial to support the proposed molecular mechanism of resistance.

In COM′, the linker is initially not in contact with the ligand (opposite of that with COM). However, after ∼20 ns, it establishes a stable link with 227G (Figure S16A of the Supporting Information). Moreover, this conformation realizes the very same closure of the RNA primer entrance found in COM (Figure S16B of the Supporting Information). Therefore, despite starting from very different structures and interaction patterns, a very similar equilibrium conformation of the complex is found, compatible with a plausible mechanism of action of 227G.[7]

In COM′m, the linker is in contact with 227G (opposite of that with COMm) at the beginning of the simulation, but after ∼15 ns, it moves to the same side of the binding pocket where it sits in COMm, losing the contacts with the L3 and linker loops (Figure S16C of the Supporting Information). Again, this situation closely resembles that found in COMm (Figure S16D of the Supporting Information), where 227G is unable to permanently occlude the RNA primer entrance gate. Moreover, this finding is independent of the orientation of the ligand, as this one is opposite in COMm and COM′m.

Obviously, one cannot exclude the presence of conformations featuring a strong contact between the linker and 227G in the mutant enzyme (and vice versa weak contact configurations could be present in the wt). However, this appears to be quite unlikely in view of the retained functionality of the mutant. Instead, we are confident that our results reflect a fundamental difference in the dynamics of the complex, which is due to the I261M mutation and is at the basis of a possible molecular mechanism of the resistance of BVDV to 227G.

Concluding Remarks. One of the major obstacles in modern drug development is the rapid acquisition of drug-resistant phenotypes, an occurrence that limits the long-term application of any drug-based therapy. Here we investigated via computer simulations the molecular mechanism of resistance of BVDV to 227G due to the I261M mutation in the RdRp protein of the virus. For this purpose, we performed an extended comparative study of the structural, dynamic, and thermodynamic properties of the wt and mutant apo- and holoenzymes. Our findings support a mechanism of BVDV RdRp inhibition due to the occlusion of the enzyme template entrance site by the ligand, similar to that recently reported by Niyomrattanakit et al.[74] for the RdRp of Dengue virus. Furthermore, we evaluated the implications of a mutation conferring resistance to 227G for the structure and dynamics of the apoenzymes and highlighted how the entrance site in the I261M variant of RdRp displays conformations in which the RNA template entrance is open as in the wt protein. Our results do not support a mechanism of resistance by impairment of inhibitor accessibility to the binding site in the mutant protein. Instead, we propose a mechanism based on the functional properties retained by the mutated RdRp bound to 227G and compatible with experimental evidence showing BVDV growth

dx.doi.org/10.1021/bi500490z | *Biochemistry* 2014, 53, 6941−6953

in the presence of the inhibitor (see Figure S17 of the Supporting Information). To the best of our knowledge, a similar mechanism of resistance has never been described in the literature.

Additional findings deserve further discussion in relation to the occurrence of resistance in the mutated RdRp. For instance, it has also been suggested that the linker is involved in recruiting the RdRp partner protein,[26,68,70] which is essential for polymerization.[26,68,70] Thus, the displacement and the larger stiffness of the linker in COM compared to those in COMm could also interfere with the assembly of the replication complex.[26,68,70] In addition, binding of 227G to motif I could even hinder the incoming NTPs at the time of polymerization. Interestingly, the flexibility of this region, compared to that of the apoenzyme, is significantly reduced in COM but not in COMm. However, also in the mutant, 227G lies on top of motif I; thus, our data cannot clearly support or discourage this last mechanism.

The results of this work can offer insights into the design of novel experiments aimed at discriminating among the resistance mechanisms proposed above. The identification of putative key residues located in crucial regions of RdRp, i.e., the template entrance site and motifs I and II, which are responsible for the high affinity of 227G, represents a valuable starting point for site-directed mutagenesis experiments followed by functional assays. Additionally, important insights might be gained by structural studies as crystallography and nuclear magnetic resonance of the mutated protein. For example, a cocrystallization of the I261M variant of RdRp with 227G might give valuable support to our proposed mechanisms.

Finally, despite the use of a thorough and promiscuous computational protocol, we cannot rule out the possibility that our findings are flawed by limitations of the various methodologies, such as poor sampling of conformational space (although the comparison of our results for COM and COM′, as well as for COMm and COM′m, points to good reproducibility of the main findings), force field inadequacies in particular in representing chemicophysical properties of the drug and/or the binding site, poor parameters for the estimation of the free energies of binding, etc. Moreover, other mechanisms not discussed in this work could be used to explain the impaired action of 227G on the resistant RdRp enzyme. For instance, if inhibition is due to competition (allosteric or not) with the RNA template, small differences in binding mode, affinity, and/or residence times could be crucial. Thus, a small difference in the free energy of binding or in the dissociation cost (related to the residence time) can be key upon comparison to those of the natural substrate of the enzyme. Nonetheless, the findings presented here confirm the experimental indication that the substitution responsible for increased resistance against NNIs occurs in the finger domain of BVDV RdRp and furnish a consistent molecular mechanism of inhibition. Ultimately, understanding the structural and functional effects of mutations can aid in the development of novel potent therapeutic agents whose activity is less susceptible to the occurrence of resistant mutants.

■ ASSOCIATED CONTENT

Supporting Information

Supplementary Figures S1−S17 and Supplementary Tables S1−S6. This material is available free of charge via the Internet at http://pubs.acs.org.

■ AUTHOR INFORMATION

Corresponding Author

*Dipartimento di Fisica, Università degli Studi di Cagliari, Cittadella Universitaria, 09042 Monserrato, CA, Italy. Telephone: +390706754911. Fax: +390706753191. E-mail: vargiu@dsf.unica.it.

Present Addresses

†S.A.: Translational Health Science and Technology Institute, Plot No. 496, phase-III, Udyog Vihar, Gurgaon, 122016 Haryana, India.

‡S.S.: 425 Washington Blvd., Jersey City, NJ 07310.

Funding

We acknowledge the financial support of MIUR via L.297/99/DM 28142 "BIOMEDICINA, Sviluppo di metodologie per la modellizzazione e lo studio di farmaci e biofarmaci", PON 2006−2009, Misura II.2, Azione a/"CYBERSAR, Cyberinfrastructure per la ricerca scientifica e tecnologica in Sardegna".

Notes

The authors declare no competing financial interest.

■ ACKNOWLEDGMENTS

A.V.V. and P.R. thank Hiroshi Nikaido (University of California, Berkeley, CA) and Andrea C. Rinaldi (University of Cagliari, Cagliari, Italy) for critical reading of the manuscript. Computer time has been provided by CASPUR, CINECA (ISCRA Grant HP10B60NPE), and CYBERSAR clusters. We also acknowledge the excellent technical support of Dr. M. Dessalvi.

■ ABBREVIATIONS

227G, 2-{1-[2-(2,4-dimethoxyphenyl)-1*H*-benzimidazol-5-yl]-ethylidene}hydrazinecarbothioamide; NNI, non-nucleoside inhibitor; NI, nucleoside inhibitor; APO, wild-type enzyme; COM, complex enzyme with 227G; HCV, hepatitis C virus; BVDV, bovine viral diarrhea virus; RdRp, RNA-dependent RNA polymerase; NS5B, nonstructural 5B protein; peg-IFN, pegylated interferon; rmsd, root-mean-square deviation; rmsf, root-mean-square fluctuation; PDB, Protein Data Bank; WHO, World Health Organization; PCA, principal component analysis.

■ REFERENCES

(1) Lanyon, S. R., Hill, F. I., Reichel, M. P., and Brownlie, J. (2014) Bovine viral diarrhoea: Pathogenesis and diagnosis. *Vet. J. 199*, 201−209.

(2) Ridpath, J. F. (2010) Bovine viral diarrhea virus: Global status. *Vet. Clin. North Am.: Food Anim. Pract. 26*, 105−121.

(3) Becher, P., Orlich, M., Shannon, A., Horner, G., and Thiel, H. (1997) Phylogenetic analysis of pestiviruses from domestic and wild ruminants. *J. Gen. Virol. 78*, 1357−1366.

(4) Kalaycioglu, A. (2007) Bovine viral diarrhoea virus (BVDV) diversity and vaccination. A review. *Vet. Q. 29*, 60−67.

(5) Ridpath, J. F. (2013) Immunology of BVDV vaccines. *Biologicals 41*, 14−19.

(6) Vitale, G., Corona, P., Loriga, M., Carta, A., Paglietti, G., Giliberti, G., Sanna, G., Farci, P., Marongiu, M. E., and La Colla, P. (2012) 5-Acetyl-2-arylbenzimidazoles as antiviral agents. Part 4. *Eur. J. Med. Chem. 53*, 83−97.

(7) Asthana, S., Shukla, S., Vargiu, A. V., Ceccarelli, M., Ruggerone, P., Paglietti, G., Marongiu, M. E., Blois, S., Giliberti, G., and La Colla, P. (2013) Different Molecular Mechanisms of Inhibition of Bovine Viral Diarrhea Virus and Hepatitis C Virus RNA-Dependent RNA Polymerases by a Novel Benzimidazole. *Biochemistry 52*, 3752−3764.

(8) Puerstinger, G., Paeshuyse, J., De Clercq, E., and Neyts, J. (2007) Antiviral 2,5-disubstituted imidazo[4,5-*c*]pyridines: From anti-pestivirus to anti-hepatitis C virus activity. *Bioorg. Med. Chem. Lett. 17*, 390−393.
(9) Puerstinger, G., Paeshuyse, J., Heinrich, S., Mohr, J., Schraffl, N., De Clercq, E., and Neyts, J. (2007) Antiviral 2,5-disubstituted imidazo[4,5-*c*]pyridines: Further optimization of anti-hepatitis C virus activity. *Bioorg. Med. Chem. Lett. 17*, 5111−5114.
(10) Baginski, S. G., Pevear, D. C., Seipel, M., Sun, S. C. C., Benetatos, C. A., Chunduru, S. K., Rice, C. M., and Collett, M. S. (2000) Mechanism of action of a pestivirus antiviral compound. *Proc. Natl. Acad. Sci. U.S.A. 97*, 7981−7986.
(11) King, R. W., Scarnati, H. T., Priestley, E. S., De Lucca, I., Bansal, A., and Williams, J. K. (2002) Selection of a thiazole urea-resistant variant of bovine viral diarrhoea virus that maps to the RNA-dependent RNA polymerase. *Antiviral Chem. Chemother. 13*, 315.
(12) Sun, J.-H., Lemm, J. A., O'Boyle, D. R., Racela, J., Colonno, R., and Gao, M. (2003) Specific inhibition of bovine viral diarrhea virus replicase. *J. Virol. 77*, 6753−6760.
(13) Tonelli, M., Simone, M., Tasso, B., Novelli, F., Boido, V., Sparatore, F., Paglietti, G., Pricl, S., Giliberti, G., and Blois, S. (2010) Antiviral activity of benzimidazole derivatives. II. Antiviral activity of 2-phenylbenzimidazole derivatives. *Bioorg. Med. Chem. 18*, 2937−2953.
(14) Giliberti, G., Ibba, C., Marongiu, E., Loddo, R., Tonelli, M., Boido, V., Laurini, E., Posocco, P., Fermeglia, M., and Pricl, S. (2010) Synergistic experimental/computational studies on arylazoenamine derivatives that target the bovine viral diarrhea virus RNA-dependent RNA polymerase. *Bioorg. Med. Chem. 18*, 6055−6068.
(15) Tonelli, M., Vettoretti, G., Tasso, B., Novelli, F., Boido, V., Sparatore, F., Busonera, B., Ouhtit, A., Farci, P., and Blois, S. (2011) Acridine derivatives as anti-BVDV agents. *Antiviral Res. 91*, 133−141.
(16) Castro, E. F., Fabian, L. E., Caputto, M. a. E., Gagey, D., Finkielsztein, L. M., Moltrasio, G. Y., Moglioni, A. G., Campos, R. H., and Cavallaro, L. a. V. (2011) Inhibition of bovine viral diarrhea virus RNA synthesis by thiosemicarbazone derived from 5,6-dimethoxy-1-indanone. *J. Virol. 85*, 5436−5445.
(17) Salim, M. T., Goto, Y., Hamasaki, T., Okamoto, M., Aoyama, H., Hashimoto, Y., Musiu, S., Paeshuyse, J., Neyts, J., and Froeyen, M. (2010) Highly potent and selective inhibition of bovine viral diarrhea virus replication by γ-carboline derivatives. *Antiviral Res. 88*, 263−268.
(18) Vitale, G., Corona, P., Loriga, M., Carta, A., Paglietti, G., Ibba, C., Giliberti, G., Loddo, R., Marongiu, E., and La Colla, P. (2010) Styrylbenzimidazoles. Synthesis and Biological Activity-Part 3. *Med. Chem. 6*, 70−78.
(19) Carta, A., Briguglio, I., Piras, S., Corona, P., Boatto, G., Nieddu, M., Giunchedi, P., Marongiu, M. E., Giliberti, G., and Iuliano, F. (2011) Quinoline tricyclic derivatives. Design, synthesis and evaluation of the antiviral activity of three new classes of RNA-dependent RNA polymerase inhibitors. *Bioorg. Med. Chem. 19*, 7070−7084.
(20) Peduto, A., Massa, A., Di Mola, A., de Caprariis, P., La Colla, P., Loddo, R., Altamura, S., Maga, G., and Filosa, R. (2011) 2,3-Dihydro-1,2-Diphenyl-substituted 4H-Pyridinone Derivatives as New Anti Flaviviridae Inhibitors. *Chem. Biol. Drug Des. 77*, 441−449.
(21) Mazzei, M., Nieddu, E., Miele, M., Balbi, A., Ferrone, M., Fermeglia, M., Mazzei, M. T., Pricl, S., La Colla, P., and Marongiu, F. (2008) Activity of Mannich bases of 7-hydroxycoumarin against Flaviviridae. *Bioorg. Med. Chem. 16*, 2591−2605.
(22) Tonelli, M., Boido, V., Canu, C., Sparatore, A., Sparatore, F., Paneni, M. S., Fermeglia, M., Pricl, S., La Colla, P., and Casula, L. (2008) Antimicrobial and cytotoxic arylazoenamines. Part III: Antiviral activity of selected classes of arylazoenamines. *Bioorg. Med. Chem. 16*, 8447−8465.
(23) Carta, A., Loriga, M., Paglietti, G., Ferrone, M., Fermeglia, M., Pricl, S., Sanna, T., Ibba, C., La Colla, P., and Loddo, R. (2007) Design, synthesis, and preliminary in vitro and in silico antiviral activity of [4,7]phenantrolines and 1-oxo-1,4-dihydro-[4,7]phenantrolines against single-stranded positive-sense RNA genome viruses. *Bioorg. Med. Chem. 15*, 1914−1927.
(24) Paeshuyse, J., Chezal, J.-M., Froeyen, M., Leyssen, P., Dutartre, H., Vrancken, R., Canard, B., Letellier, C., Li, T., Mittendorfer, H., et al. (2007) The imidazopyrrolopyridine analogue AG110 is a novel, highly selective inhibitor of pestiviruses that targets the viral RNA-dependent RNA polymerase at a hot spot for inhibition of viral replication. *J. Virol. 81*, 11046−11053.
(25) Paeshuyse, J., Leyssen, P., Mabery, E., Boddeker, N., Vrancken, R., Froeyen, M., Ansari, I. H., Dutartre, H., Rozenski, J., and Gil, L. H. (2006) A novel, highly selective inhibitor of pestivirus replication that targets the viral RNA-dependent RNA polymerase. *J. Virol. 80*, 149−160.
(26) Choi, K. H., Groarke, J. M., Young, D. C., Kuhn, R. J., Smith, J. L., Pevear, D. C., and Rossmann, M. G. (2004) The structure of the RNA-dependent RNA polymerase from bovine viral diarrhea virus establishes the role of GTP in de novo initiation. *Proc. Natl. Acad. Sci. U.S.A. 101*, 4425−4430.
(27) Humphrey, W., Dalke, A., and Schulten, K. (1996) VMD: Visual molecular dynamics. *J. Mol. Graphics 14*, 33−38.
(28) Frisch, M. J., Trucks, G. W., Schlegel, H. B., Scuseria, G. E., Robb, M. A., Cheeseman, J. R., Montgomery, J. A., Jr., Vreven, T., Kudin, K. N., Burant, J. C., Millam, J. M., Iyengar, S. S., Tomasi, J., Barone, V., Mennucci, B., Cossi, M., Scalmani, G., Rega, N., Petersson, G. A., Nakatsuji, H., Hada, M., Ehara, M., Toyota, K., Fukuda, R., Hasegawa, J., Ishida, M., Nakajima, T., Honda, Y., Kitao, O., Nakai, H., Klene, M., Li, X., Knox, J. E., Hratchian, H. P., Cross, J. B., Bakken, V., Adamo, C., Jaramillo, J., Gomperts, R., Stratmann, R. E., Yazyev, O., Austin, A. J., Cammi, R., Pomelli, C., Ochterski, J. W., Ayala, P. Y., Morokuma, K., Voth, G. A., Salvador, P., Dannenberg, J. J., Zakrzewski, V. G., Dapprich, S., Daniels, A. D., Strain, M. C., Farkas, O., Malick, D. K., Rabuck, A. D., Raghavachari, K., Foresman, J. B., Ortiz, J. V., Cui, Q., Baboul, A. G., Clifford, S., Cioslowski, J., Stefanov, B. B., Liu, G., Liashenko, A., Piskorz, P., Komaromi, I., Martin, R. L., Fox, D. J., Keith, T., Al-Laham, M. A., Peng, C. Y., Nanayakkara, A., Challacombe, M., Gill, P. M. W., Johnson, B., Chen, W., Wong, M. W., Gonzalez, C., and Pople, J. A. (2004) *Gaussian 03*, revision C.02, Gaussian, Inc., Wallingford, CT.
(29) Morris, G. M., Huey, R., Lindstrom, W., Sanner, M. F., Belew, R. K., Goodsell, D. S., and Olson, A. J. (2009) AutoDock4 and AutoDockTools4: Automated docking with selective receptor flexibility. *J. Comput. Chem. 30*, 2785−2791.
(30) Phillips, J. C., Braun, R., Wang, W., Gumbart, J., Tajkhorshid, E., Villa, E., Chipot, C., Skeel, R. D., Kale, L., and Schulten, K. (2005) Scalable molecular dynamics with NAMD. *J. Comput. Chem. 26*, 1781−1802.
(31) Lindorff-Larsen, K., Piana, S., Palmo, K., Maragakis, P., Klepeis, J. L., Dror, R. O., and Shaw, D. E. (2010) Improved side-chain torsion potentials for the Amber ff99SB protein force field. *Proteins: Struct., Funct., Bioinf. 78*, 1950−1958.
(32) Aaqvist, J. (1990) Ion-water interaction potentials derived from free energy perturbation simulations. *J. Phys. Chem. 94*, 8021−8024.
(33) Joung, I. S., and Cheatham, T. E., III (2008) Determination of alkali and halide monovalent ion parameters for use in explicitly solvated biomolecular simulations. *J. Phys. Chem. B 112*, 9020−9041.
(34) Wang, J., Wolf, R. M., Caldwell, J. W., Kollman, P. A., and Case, D. A. (2004) Development and testing of a general amber force field. *J. Comput. Chem. 25*, 1157−1174.
(35) Bayly, C. I., Cieplak, P., Cornell, W., and Kollman, P. A. (1993) A well-behaved electrostatic potential based method using charge restraints for deriving atomic charges: The RESP model. *J. Phys. Chem. 97*, 10269−10280.
(36) Andersen, H. C. (1980) Molecular dynamics simulations at constant pressure and/or temperature. *J. Chem. Phys. 72*, 2384−2393.
(37) Parrinello, M., and Rahman, A. (1981) Polymorphic transitions in single crystals: A new molecular dynamics method. *J. Appl. Phys. 52*, 7182−7190.
(38) Hoover, W. G. (1985) Canonical dynamics: Equilibrium phase-space distributions. *Phys. Rev. A 31*, 1695.
(39) Nosé, S. (1984) A molecular dynamics method for simulations in the canonical ensemble. *Mol. Phys. 52*, 255−268.

(40) Essmann, U., Perera, L., Berkowitz, M. L., Darden, T., Lee, H., and Pedersen, L. G. (1995) A smooth particle mesh Ewald method. *J. Chem. Phys. 103*, 8577−8593.
(41) Paeshuyse, J., Letellier, C., Froeyen, M., Dutartre, H., Vrancken, R., Canard, B., De Clercq, E., Gueiffier, A., Teulade, J.-C., and Herdewijn, P. (2009) A pyrazolotriazolopyrimidinamine inhibitor of bovine viral diarrhea virus replication that targets the viral RNA-dependent RNA polymerase. *Antiviral Res. 82*, 141−147.
(42) Amaro, R. E., Baron, R., and McCammon, J. A. (2008) An improved relaxed complex scheme for receptor flexibility in computer-aided drug design. *J. Comput.-Aided Mol. Des. 22*, 693−705.
(43) Daura, X., Gademann, K., Jaun, B., Seebach, D., van Gunsteren, W. F., and Mark, A. E. (1999) Peptide folding: When simulation meets experiment. *Angew. Chem., Int. Ed. 38*, 236−240.
(44) Hess, B., Kutzner, C., Van Der Spoel, D., and Lindahl, E. (2008) GROMACS 4: Algorithms for highly efficient, load-balanced, and scalable molecular simulation. *J. Chem. Theory Comput. 4*, 435−447.
(45) Porollo, A., and Meller, J. (2010) POLYVIEW-MM: Web-based platform for animation and analysis of molecular simulations. *Nucleic Acids Res. 38*, W662−W666.
(46) Coleman, R. G., and Sharp, K. A. (2009) Finding and characterizing tunnels in macromolecules with application to ion channels and pores. *Biophys. J. 96*, 632−645.
(47) Kumar, A., Hajjar, E., Ruggerone, P., and Ceccarelli, M. (2010) Molecular simulations reveal the mechanism and the determinants for ampicillin translocation through OmpF. *J. Phys. Chem. B 114*, 9608−9616.
(48) Felluga, F., Fermeglia, M., Ferrone, M., Pitacco, G., Pricl, S., and Valentin, E. (2002) Computational studies on the enantioselectivity of α-chymotrypsin towards β-carbomethoxy-γ-lactams. *Tetrahedron: Asymmetry 13*, 475−489.
(49) Amadei, A., Linssen, A., and Berendsen, H. J. (1993) Essential dynamics of proteins. *Proteins: Struct., Funct., Bioinf. 17*, 412−425.
(50) Daidone, I., and Amadei, A. (2012) Essential dynamics: Foundation and applications. *WIREs Computational Molecular Science 2*, 762−770.
(51) García, A. E. (1992) Large-amplitude nonlinear motions in proteins. *Phys. Rev. Lett. 68*, 2696.
(52) Fogolari, F., Brigo, A., and Molinari, H. (2002) The Poisson-Boltzmann equation for biomolecular electrostatics: A tool for structural biology. *J. Mol. Recognit. 15*, 377−392.
(53) Kollman, P. A., Massova, I., Reyes, C., Kuhn, B., Huo, S., Chong, L., Lee, M., Lee, T., Duan, Y., and Wang, W. (2000) Calculating structures and free energies of complex molecules: Combining molecular mechanics and continuum models. *Acc. Chem. Res. 33*, 889−897.
(54) Vargiu, A. V., Ruggerone, P., Magistrato, A., and Carloni, P. (2008) Sliding of alkylating anticancer drugs along the minor groove of DNA: New insights on sequence selectivity. *Biophys. J. 94*, 550−561.
(55) Hou, T., Wang, J., Li, Y., and Wang, W. (2011) Assessing the performance of the MM/PBSA and MM/GBSA methods. 1. The accuracy of binding free energy calculations based on molecular dynamics simulations. *J. Chem. Inf. Model. 51*, 69−82.
(56) Rocchia, W., Sridharan, S., Nicholls, A., Alexov, E., Chiabrera, A., and Honig, B. (2002) Rapid grid-based construction of the molecular surface and the use of induced surface charge to calculate reaction field energies: Applications to the molecular systems and geometric objects. *J. Comput. Chem. 23*, 128−137.
(57) Kongsted, J., and Ryde, U. (2009) An improved method to predict the entropy term with the MM/PBSA approach. *J. Comput.-Aided Mol. Des. 23*, 63−71.
(58) Gohlke, H., Kiel, C., and Case, D. A. (2003) Insights into protein-protein binding by binding free energy calculation and free energy decomposition for the Ras-Raf and Ras-RalGDS complexes. *J. Mol. Biol. 330*, 891−913.
(59) Vargiu, A. V., and Nikaido, H. (2012) Multidrug binding properties of the AcrB efflux pump characterized by molecular dynamics simulations. *Proc. Natl. Acad. Sci. U.S.A. 109*, 20637−20642.
(60) Lin, J.-H., Perryman, A. L., Schames, J. R., and McCammon, J. A. (2002) Computational drug design accommodating receptor flexibility: The relaxed complex scheme. *J. Am. Chem. Soc. 124*, 5632−5633.
(61) Andrusier, N., Mashiach, E., Nussinov, R., and Wolfson, H. J. (2008) Principles of flexible protein-protein docking. *Proteins: Struct., Funct., Bioinf. 73*, 271−289.
(62) B-Rao, C., Subramanian, J., and Sharma, S. D. (2009) Managing protein flexibility in docking and its applications. *Drug Discovery Today 14*, 394−400.
(63) Cozzini, P., Kellogg, G. E., Spyrakis, F., Abraham, D. J., Costantino, G., Emerson, A., Fanelli, F., Gohlke, H., Kuhn, L. A., and Morris, G. M. (2008) Target Flexibility: An Emerging Consideration in Drug Discovery and Design. *J. Med. Chem. 51*, 6237−6255.
(64) May, A., Sieker, F., and Zacharias, M. (2008) How to efficiently include receptor flexibility during computational docking. *Curr. Comput.-Aided Drug Des. 4*, 143−153.
(65) Wang, C., Bradley, P., and Baker, D. (2007) Protein-protein docking with backbone flexibility. *J. Mol. Biol. 373*, 503−519.
(66) Bressanelli, S., Tomei, L., Rey, F. A., and De Francesco, R. (2002) Structural analysis of the hepatitis C virus RNA polymerase in complex with ribonucleotides. *J. Virol. 76*, 3482−3492.
(67) Bressanelli, S., Tomei, L., Roussel, A., Incitti, I., Vitale, R. L., Mathieu, M., De Francesco, R., and Rey, F. A. (1999) Crystal structure of the RNA-dependent RNA polymerase of hepatitis C virus. *Proc. Natl. Acad. Sci. U.S.A. 96*, 13034−13039.
(68) Choi, K. H., Gallei, A., Becher, P., and Rossmann, M. G. (2006) The structure of bovine viral diarrhea virus RNA-dependent RNA polymerase and its amino-terminal domain. *Structure 14*, 1107−1113.
(69) Xiao, M., Li, H., Wang, Y., Wang, X., Wang, W., Peng, J., Chen, J., and Li, B. (2006) Characterization of the N-terminal domain of classical swine fever virus RNA-dependent RNA polymerase. *J. Gen. Virol. 87*, 347−356.
(70) Choi, K. H., and Rossmann, M. G. (2009) RNA-dependent RNA polymerases from *Flaviviridae*. *Curr. Opin. Struct. Biol. 19*, 746−751.
(71) Kim, Y.-C., Russell, W. K., Ranjith-Kumar, C., Thomson, M., Russell, D. H., and Kao, C. C. (2005) Functional analysis of RNA binding by the hepatitis C virus RNA-dependent RNA polymerase. *J. Biol. Chem. 280*, 38011−38019.
(72) Lai, V. C., Kao, C. C., Ferrari, E., Park, J., Uss, A. S., Wright-Minogue, J., Hong, Z., and Lau, J. Y. (1999) Mutational analysis of bovine viral diarrhea virus RNA-dependent RNA polymerase. *J. Virol. 73*, 10129−10136.
(73) Harrus, D., Ahmed-El-Sayed, N., Simister, P. C., Miller, S., Triconnet, M., Hagedorn, C. H., Mahias, K., Rey, F. A., Astier-Gin, T., and Bressanelli, S. (2010) Further insights into the roles of GTP and the C terminus of the hepatitis C virus polymerase in the initiation of RNA synthesis. *J. Biol. Chem. 285*, 32906−32918.
(74) Niyomrattanakit, P., Chen, Y.-L., Dong, H., Yin, Z., Qing, M., Glickman, J. F., Lin, K., Mueller, D., Voshol, H., and Lim, J. Y. (2010) Inhibition of dengue virus polymerase by blocking of the RNA tunnel. *J. Virol. 84*, 5678−5686.
(75) Yap, T. L., Xu, T., Chen, Y.-L., Malet, H., Egloff, M.-P., Canard, B., Vasudevan, S. G., and Lescar, J. (2007) Crystal structure of the dengue virus RNA-dependent RNA polymerase catalytic domain at 1.85-angstrom resolution. *J. Virol. 81*, 4753−4765.